Materials and Design 143 (2018) 268–273

Contents lists available at ScienceDirect

Materials and Design

journal homepage: www.elsevier.com/locate/matdes

Experimental realisation of off-stoichiometric Fe-Mn-Si full Heusler alloy with hexagonal crystal structure by pulsed laser deposition

N.R. Checca[a,b], R.J. Caraballo-Vivas[a,b], A.A. Coelho[c], A. Rossi[b], N.M. Fortunato[d], F. Mohseni[d,e], J.N. Gonçalves[d], J.S. Amaral[d], D.L. Rocco[a], M.S. Reis[a,f,*]

[a] Institute of Physics, Fluminense Federal University, Av. Gal. Milton Tavares de Souza s/n, 24210-346 Niterói, RJ, Brazil
[b] Brazilian Center for Research in Physics, R. Dr. Xavier Sigaud 150, 22290-180 Rio de Janeiro, RJ, Brazil
[c] Institute of Physics - Gleb Wataghin, Campinas State University - Unicamp, 13083-859 Campinas, SP, Brazil
[d] Department of Physics and CICECO - Aveiro Institute of Materials, University of Aveiro, Aveiro 3810-193, Portugal
[e] Department of Materials and Ceramic Engineering and CICECO - Aveiro Institute of Materials, University of Aveiro, Aveiro 3810-193, Portugal
[f] Department of Physics and I3N, University of Aveiro, Aveiro 3810-193, Portugal

HIGHLIGHTS

- Nanoparticles of Fe-Mn-Si full Heusler alloys, produced by pulsed laser deposition, present an hexagonal structure.
- Density functional calculations ratify the energy minima for this hexagonal structure.
- Due to the magneto-structural coupling on these materials, the Curie temperature increases 25%.
- These results open doors for new physical properties of Heusler alloys.

GRAPHICAL ABSTRACT

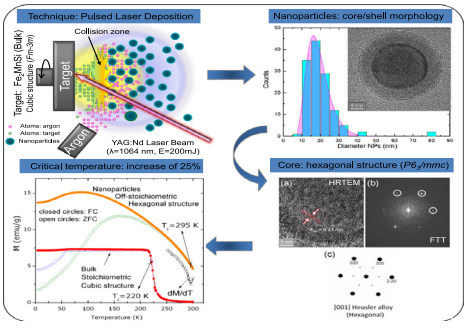

ARTICLE INFO

Article history:
Received 8 September 2017
Received in revised form 29 January 2018
Accepted 30 January 2018
Available online 10 February 2018

Keywords:
Nanoparticles
Pulsed laser deposition
Heusler alloys
Structural change

ABSTRACT

Full Heusler alloys are well known to either crystallize in a cubic structure (Cu_2MnAl-type), or present tetragonal distortions. Both structure types present interesting properties, like room temperature magnetic memory shape effect and/or remarkable magnetocaloric effect, mainly ruled by strong magnetostructural coupling. Due to this interplay, our aim was to produce a new crystal phase for the Heusler alloys, different from those well-established cubic and tetragonal, responsible for those well-known physical properties. Thus, we have produced nanoparticles of full Heusler alloys using a pulsed laser deposition technique (from targets of Fe_2MnSi) and obtained a core-shell pattern, presenting an amorphous shell and a crystalline core, with hexagonal symmetry. In accordance with these experimental findings, it was shown, by means of density functional calculation, the existence of a minimum of energy as a function of the hexagonal lattice parameters, with a true indication that the hexagonal phase is metastable. The magnetic properties differ considerably from those of bulk Fe_2MnSi, including an increase of the Curie temperature from 220 K to 295 K, which is of potential interest for room-temperature applications. This work opens the door to research in a new family of materials, whose properties have only now begun to be explored.

1. Introduction

Heusler alloys are multifunctional materials, with extraordinary properties and a large amount of potential application in technological devices. Just to name a few, we can cite the magnetic

* Corresponding author at: Institute of Physics, Fluminense Federal University, Av. Gal. Milton Tavares de Souza s/n, Niterói 24210-346, RJ, Brazil.
E-mail address: marior@if.uff.br (M. Reis).

https://doi.org/10.1016/j.matdes.2018.01.062
0264-1275/

transition close to room temperature, finely tuned to work in cooperation with the first order structural transition in the same temperature region [1]. This fact pushes this material to the top of the list of the most promising ones to be used as active magnetic regenerator in magnetocaloric devices [2]. We can also cite the shape-memory effect [3], in which some Heusler alloys undergo a mechanical transformation due to a thermal and/or magnetic field excitation. These kind of materials could replace pneumatic, electromagnetic and hydraulic drives in several devices; with the great advantage to be fast and precise under control by the magnetic field [4]. In spite of appearing to be independent phenomena, these examples are absolutely interconnected [5]; and this interplay of physical properties is the key role for the astonishing characteristics of the Heusler alloys. We can go beyond and cite some other important properties, such as: variable electronic structure, e.g., half-metallic ferromagnetism[6] and superconductivity [7]. Applications on solar cells [8] and topological insulators [9] are also discussed on the literature.

Heusler alloys are of the type X_2YZ (Cu_2MnAl-type structure - full Heusler) or XYZ (MgAgAs type-structure - half Heusler), where X and Y are transition metals and Z belongs to either post-transition metals or metalloid groups [10]. Stoichiometric X_2YZ *ternary* compositions with $L2_1$ symmetry crystallize in Cu_2MnAl cubic structure with the space group $Fm\bar{3}m$, which is formed by four interpenetrating *fcc* sub-lattices. Two of these sub-lattices are occupied by X ions in the 8*c* (1/4,1/4,1/4) position, and the other two sub-lattices occupied by Y and Z ions in 4*a* (0,0,0) and 4*b* (1/2,1/2,1/2) positions, respectively. However, changes on this structure, still considering the stoichiometric composition, can be found due to atomic disorder, i.e., interchanges between the X, Y and/or Z ions. One of these changes leads to the $D0_3$ structure (X ions exchange position with Y ions); and it has consequences on the physical properties of the material, as already discussed by Vidal and co-workers [11], which pointed out that this change of structure has an impact on the anomalous Hall effect. However, considering the *ternary* compositions, the most relevant physical properties (mediated by the magneto-structural coupling above described and experimentally tuned to work in benefit of devices), are found on off-stoichiometric compositions; such as the magnetocaloric $Ni_{2.2}Mn_{0.8}Ga$ and $Ni_{2.1}Mn_{0.7}Ga$ compounds [1,12] and the magnetic-field induced strain and large magnetothermal conductive $Ni_{50}Mn_{50-x}In_x$ compositions [13].

On the other hand, structural changes can be found on the *binary* Mn_2MnZ (Z = Ga and Ge), that can be packed in hexagonal, tetragonal or cubic phases (either bulk or thin films) [14–17]; and a special attention must be given to the case of Mn_3Ga, which assumes a hexagonal structure [14]. The transformation from the cubic phase to the hexagonal one was also observed in Fe_3Ge above 700 K [18]. These are examples of alloys, *similar* to the full Heusler 2:1:1, that present further transitions to other crystal structures, as the hexagonal one; however, these are binary.

Considering thus that the crystal structure plays an important role on the physical properties of these materials, our goal is to produce a *ternary* alloy with other symmetry, in order to uncover new physical effects and new magneto-structural correlations. We achieved this goal by producing core-shell nanoparticles (NPs) of Fe_2MnSi (nominal concentration) by means of Pulsed Laser Deposition (PLD) technique. We found a crystalline core with hexagonal structure and an off-stoichiometric composition of Fe-Mn-Si Heusler alloy. From these achievements, the scientific community will be able to assess many open questions, like: the dependence of the physical properties of Heusler alloys with other (i) crystal packing and (ii) sample size; (iii) whether the high spin polarization or its half-metallic feature can be preserved in low dimension [19]; and many other issues.

2. Experimental and theoretical details

The polycrystalline target of Fe_2MnSi (nominal composition, $L2_1$ cubic structure) was obtained using conventional arc furnace technique, melted from a stoichiometric amount of iron, manganese (with an excess of 3% due to losses on melting [20]) and silicon. To ensure the homogenization of the 4 g target, it was sealed in a quartz tube, filled with Ar gas, annealed during 3 days at 1373 K and then quenched in water.

We have produced the NPs using a home-made Pulsed Laser Deposition (PLD), which is a technique for deposition of NPs in liquid media and in chambers with high gas pressures (~1 Torr). In the latter, plume expansion through the gas occurs, being a phenomenon much more complex than an expansion through the vacuum. The gas affects the plume dynamics and the spatial distribution and kinetic-energy distribution of atoms, ions and molecules, influencing NP nucleation and formation on-the-flight. These nanostructures formed by PLD are used for different applications such as solar cells [21,22], reflective coatings [23], photocatalysis [24,25], just to mention a few [26–28]. Our devices uses a Nd:YAG laser with the following characteristic: wavelength of $\lambda = 1064$ nm; 7 ns of pulse duration; 10 Hz of repetition rate; and 200 mJ of energy per pulse. The substrate-target distance was 3 cm and, for deposition, the laser beam was focused on the target in the presence of an Ar buffer atmosphere of 1 Torr. A throughout description of the deposition procedure of this material was reported by some of us in reference [29]. These samples were prepared at IF-UFF.

Transmission Electron Microscopy (TEM) measurements were performed on a high resolution mode in a field emission JEOL 2100F, operated at 200 kV and equipped with a Noran 7 Energy Dispersive Spectroscopy detector. These measurements were made at CBPF-LABNANO. The magnetic properties were measured using a commercial Superconducting Quantum Interference Device (SQUID, from Quantum Design, model MPMS-XL), at IF-UNICAMP.

Complementary Density Functional Theory (DFT) calculations were performed to better understand the hexagonal phase experimentally found. These calculations were made using the PBE functional [30], as implemented in the Wien2 K package [31], that uses the linearized augmented plane-wave + local orbitals (LAPW + lo) method. The RK_{max} parameter was set at 7.98, where RK_{max} is the product of the smallest atomic sphere by the largest $K-$vector in the plane wave expansion of the wave function. A total of 168 $k-$points in the Brillouin zone were considered. For these DFT calculations, the structure considered was a Mn_3Ga-like ($P6_3/mmc$ space group). Fe and Mn ions occupy the Mn site; while Si occupies the Ga site. To deal with the disorder, the Virtual Crystal Approximation was used [32]. One hexagonal unit cell comprised of 8 atoms was considered, together with periodic boundary conditions. These calculations were made at CICECO-UA.

3. Results and discussion

3.1. Transmission electron microscopy: morphology, crystallography and composition

To present our findings, let us start with a description of the morphology of the Fe-Mn-Si NPs, followed by a comprehensive description of their crystal structure and magnetic behavior. Thus, to better understand the morphology of these NPs, we used transmission electron microscopy (TEM). To achieve this goal, these NPs were deposited directly on the surface of copper grids covered by a thin carbon film. The obtained particle size distribution (PSD) is presented on Fig. 1 - result obtained from several TEM images. It is worth to note the asymmetry of the distribution. For a better

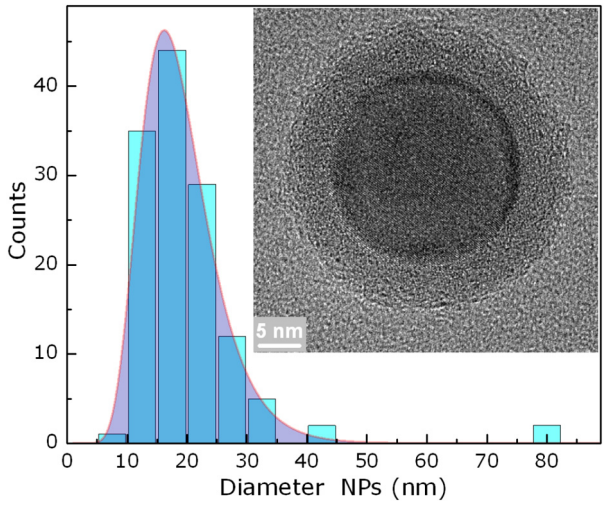

Fig. 1. Particle size distribution obtained from several images of transmission electron microscopy (TEM). The shadowed area represents the fitting of a log-normal function to the experimental data. Output parameters are on the text. Inset: typical core-shell structure found for these NPs, after a high-resolution TEM (HRTEM) acquisition.

description, we have considered a log-normal distribution to be fitted to the experimental data:

$$f(D) = \frac{A}{\sigma D\sqrt{2\pi}} \exp\left\{-\frac{[\ln(D)-\mu]^2}{2\sigma^2}\right\} \quad (1)$$

where A is the amplitude of the distribution and D is the NP size. Above, μ (location) and σ (scale), are parameters that define the statistical and relevant quantities of the problem, such as: standard-deviation $\Delta = \sqrt{e^{\sigma^2}-1}\; e^{\mu+\sigma^2/2}$; mean size of NPs $\langle D\rangle = e^{\mu+\sigma^2/2}$; and mode (most probable value of NPs) $D_m = e^{\mu-\sigma^2}$. The theoretical fitting to the data (solid red curve with purple shadowed area), also presented on Fig. 1, returns: $\Delta = 6.38$ nm, $\langle D\rangle = 19.00$ nm and $D_m = 16.19$ nm.

For a more detailed study of the morphology, a high-resolution transmission electron microscopy (HRTEM) has been performed; and a representative image is shown in the inset of Fig. 1. The NPs show a clear core/shell pattern, with an atomically ordered core and an atomically disordered shell. We reached these conclusions after a deeper analysis of several images similar to the on presented on Fig. 2 (a), which shows a HRTEM with a magnification of an area of the core. It is clear to see the resolved lattice planes of the core, with an inter-planar spacing of 0.23 nm. These planes could not be seen on a similar image for the shell and therefore we conclude on its atomically disordered state.

Deepening on this analysis, the Fast Fourier Transform (FFT) from that HRTEM image is shown on Fig. 2 (b). The angles between reflections were found to be 60° and all the reflections presented the same interplanar distances of $d_{hkl} = 0.23$ nm. Several different crystal structures were tried to match that FFT, as discussed below. The cubic Fe_2MnSi sample ($Fm\bar{3}m$ space group) along the [111] plane presents an hexagonal diffraction pattern; however, the {02-2} planes have an interplanar distance of 0.20 nm, different from that measured experimentally. Thus, we continued to seek for other structures with a better crystallographic matching. The tetragonal $Fe_{0.6}Mn_{0.4}Si_2$ ($P4/mmm$) and hexagonal $Fe_2Mn_3Si_3$ ($P6_3/mcm$) systems, both off-stoichiometric, present an hexagonal pattern along the [001] plane. However, the first case shows an interplanar distance of 0.20 nm in the {110} planes, while the second structure presents two families of planes: {200} and {3-20}, corresponding to interplanar distances of 0.30 nm and 0.22 nm, respectively. These two structures do not fit the one observed experimentally. On the other hand, the Mn_3Ga hexagonal structure ($P6_3/mmc$) along the [001] plane presents a good agreement with the experimental FFT pattern, as well as the distances on the {200} planes are 0.23 nm, that perfectly matches the one experimentally observed. These results show therefore that we could synthesize an hexagonal alloy.

It is worth mentioning that the hexagonal phase ($P6_3/mmc$) was found using two powerful software programs: Gatan (Digital Micrograph) [33] and JEMs (electron microscopy simulation software) [34]; and the last one houses the databases of crystalline structures (ICSD), as well as the corresponding FFT image. In addition, JEMs software is able to handle typical calculations of crystallographic data from electron microscopy and automatically index the diffraction patterns, simulation of spot, drawing of stereographic projections, calculation of the Bravais lattice of unknown structure from two diffraction patterns, etc. JEMs also offers the possibility to simulate structures with or without defects, using either a Fast-Fourier-Transform-based multi-sliced approach or the Bloch wave formalism [34].

Once this hexagonal structure has been confirmed by HRTEM, the hexagonal lattice parameters (a, c) could be estimated from the interplanar values (d_{hkl}) obtained from the FFT analysis of the

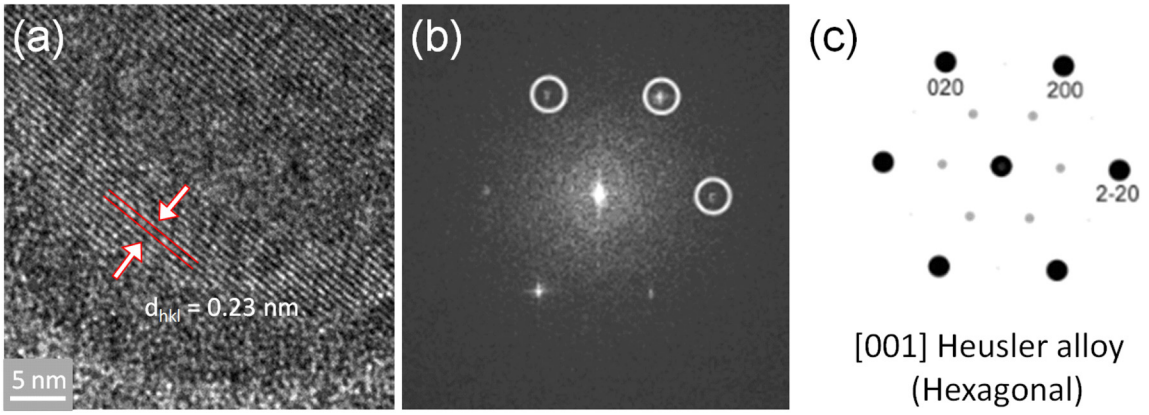

Fig. 2. (a) High-resolution transmission electron microscopy (HRTEM) magnification of an area of the core. (b) Fast Fourier Transform (FFT) of the area highlighted in (a). (c) Theoretical pattern from Mn_3Ga hexagonal structure along the [001] plane, space group $P6_3/mmc$. This theoretical pattern matches the experimental one. See the text for further details.

Table 1
Interplanar spacing values measured from HRTEM images of different NPs.

Planes	d_{hkl} (nm)
{200}	0.230
{$\bar{1}$20}	0.266
{220}	0.132
{102}	0.205

HRTEM images. For hexagonal systems, the relationship between the interplanar distance and the lattice parameters is given by:

$$\frac{1}{d_{hkl}} = \frac{4}{3}\frac{h^2 + k^2 + hk}{a^2} + \frac{l^2}{c^2}. \quad (2)$$

From several HRTEM images, a set of interplanar distances were obtained, as detailed in Table 1; and using these d_{hkl} lattice spacing values into Eq. (2), the lattice parameters could be estimated: $a = 5.30 \pm 0.02$ Å and $c = 4.58 \pm 0.02$ Å.

From an Energy Dispersive Spectroscopy (EDS) measurement, performed on a Scanning Electron Microscope (SEM), we could verify that the bulk target, with nominal composition of Fe_2MnSi, has a real composition close to the nominal one of $Fe_{2.00}Mn_{0.96}Si_{0.85}$. The procedure to prepare these NPs; roughly described above, but detailed described in reference [29], produced an off-stoichiometric material. We could not precisely determine the stoichiometry of the core due to technical reasons, particularly the influence of the shell when measuring the core, and the non-homogeneity of the NPs. However, our qualitative EDS results surely points toward an off-stoichiometric composition with a richer iron content in comparison to the nominal concentration.

Thus, this experimental procedure was able to produce an off-stoichiometric full Heusler alloy with hexagonal symmetry within the space group $P6_3/mmc$. It is a surprising result, since these *ternary* materials are widely known as either cubic or tetragonal [10]. Considering that most of the extraordinary physical properties of these materials have a strong structural dependence, we claim that this crystal change can possibly lead to significant new changes on the physical properties of this new Heusler alloy. Below, we will discuss the magnetic behavior of this material and, following this study, we will show, by first principle studies, that in fact this hexagonal phase is stable - to ratify our findings. From now on will call these two samples as hexagonal (NPs) and cubic (bulk).

3.2. Magnetic measurements

Magnetization as a function of temperature was measured for both samples: target (bulk, cubic, stoichiometric) and the NPs (hexagonal, off-stoichiometric), as presented on Fig. 3 (a). Zero field cooled-ZFC and field cooled-FC standard protocols were performed; and it is possible to observe a huge difference between those two curves. There are some reasons for the huge difference of these curves: (i) the target sample is in bulk shape, while for the NPs, the superparamagnetic regime emerges; (ii) the stoichiometric factor; and (iii) the cubic and hexagonal structures. It is important to stress that the down turn on the ZFC curve, at 50 K, for the target sample is due to an antiferromagnetic arrangement of Mn ions - information obtained by neutron diffraction and DFT calculations [35,36]. However, the most interesting result is the clear increase of the Curie temperature, from 220 K (for the bulk sample), to 295 K (for the core of the NPs) - values obtained from the inflection point of the $M(T)$ curve, as can be observed on Fig. 3 (a). This change of Curie temperature by 75 K, c.a. 25.4%, is a consequence of both crystal change from cubic to hexagonal and stoichiometry.

A deeper analysis of these results allow us to confirm the superparamagnetic behavior of these NPs. Mamiya and co-workers [37] developed a model to extract the blocking temperature distribution from the temperature derivative of the difference between the ZFC and FC curves; and after this procedure (normalized by a constant), we could obtain this quantity, depicted on Fig. 3 (b). Note it has two peaks, one at 22 K and other at 97 K; and the tail of the distribution completely disappears at 275 K. The superparamagnetic specimen is characterized by a blocking temperature T_B, above which the NPs are free to rotate; and below which these NPs are frozen along a certain direction, producing therefore a magnetic hysteresis. Fig. 4 presents the magnetization as a function of the magnetic field for these materials; Fig. 4 (b) focuses on the low field region, where it is possible to see the magnetic hysteresis with a coercive field of c.a. 630 Oe at 4 K for the NPs sample (inside the T_B distribution region), and a clear disappearance of this hysteresis at room temperature (outside the T_B distribution region). These results strongly suggest the superparamagnetic regime of these NPs.

Fig. 4 (a), on the other hand, focuses on the high values of magnetization - up to 50 kOe. The target sample (in bulk shape), reaches a saturation value of 61.3 emu/g (obtained from $M(1/H)$ plot - shown on the inset of Fig. 4 (a)), corresponding to 2.1 μ_B/FU (where FU means Formula Unity); and increasing the temperature up to 300 K, above the Curie temperature (220 K), we found only a straight line, typical of a paramagnetic specimen. These results described above are for the bulk sample; but our findings are in fact different for the NPs: in addition to the magnetic hysteresis already described above to explain the superparamagnetic state -see Fig. 4 (b)- we found a magnetic saturation of 54.2 emu/g, corresponding to 1.9 μ_B/FU. However, this value of magnetic saturation does not correspond

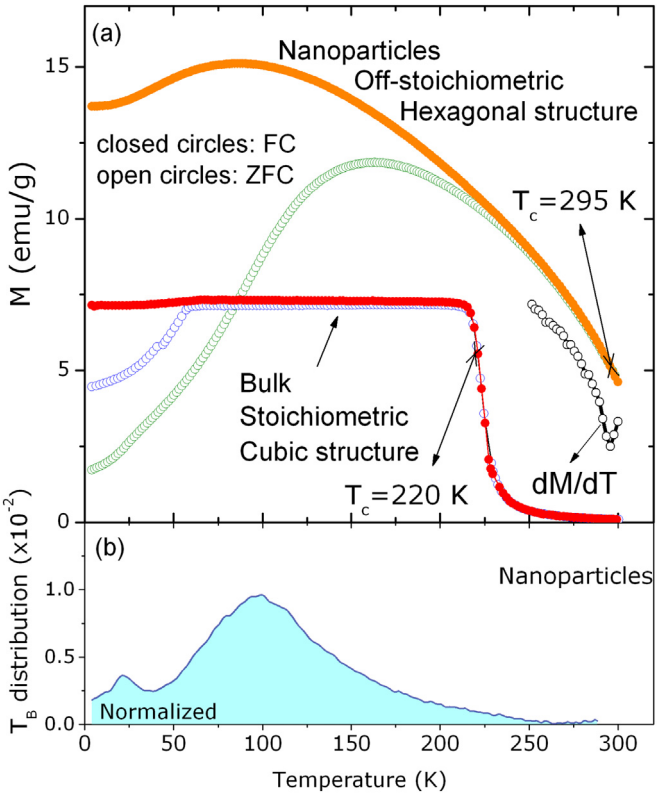

Fig. 3. (a) ZFC and FC standard protocols for the nanoparticles (hexagonal) and the bulk (cubic) Heusler alloys. It is worth to note the increasing of the Curie temperature from 220 K (target) to 295 K (core of the nanoparticles); c.a. 25%. The temperature derivative of the nanoparticles magnetization is also presented to ensure the visualization of the Curie point. (b) Blocking temperature distribution, obtained from the temperature derivative of the difference between the ZFC and FC curves [37].

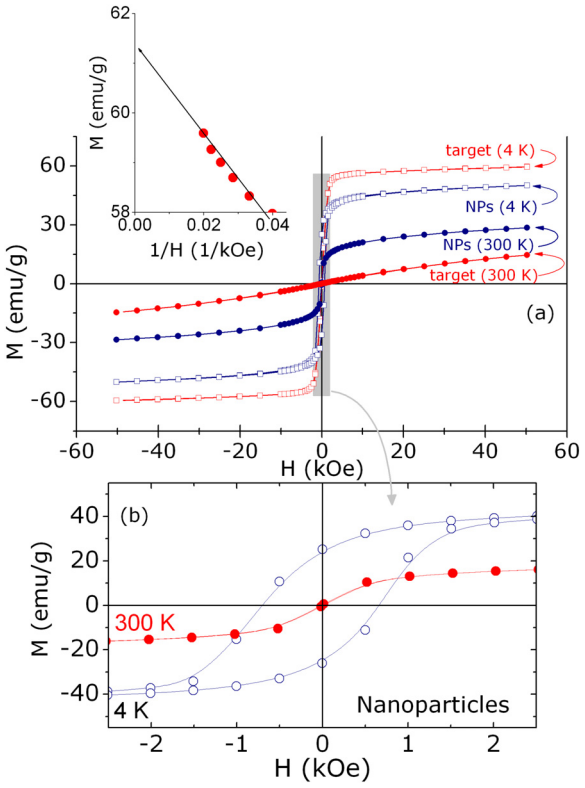

Fig. 4. (a) High field magnetization measurement, up to 50 kOe, for both nanoparticles and target. These measurements were carried out at 4 K and 300 K. Inset: magnetization as a function of the reciprocal magnetic field to extrapolate the saturation value of the magnetization. (b) Magnification of the low values of magnetic field to highlight the hysteresis found at 4 K (within the blocking temperature region -see Fig. 3 (b)), for the NPs. Considering that at 300 K (outside of the blocking temperature region), this hysteresis is no longer observed, we concluded, in fact, that these NPs are in the superparamagnetic regime.

to only the hexagonal phase, because the NPs have a core-shell morphology and a fraction of the amorphous shell (and possibly non-magnetic) is contributing to the mass of the whole sample.

Other physical properties, in addition to these already studied, deserve to be further explored to deeply increase our knowledge on this interplay between the hexagonal packing of ions and the corresponding physical mechanisms.

3.3. Density Functional Theory calculations

DFT calculations were also carried out to verify the possibility of a (meta-)stable hexagonal structure for both the stoichiometric and off-stoichiometric compositions. We have considered $Fe_{2.4}Mn_{0.6}Si$ as an off-stoichiometric composition. To achieve this goal, the minimization of the lattice parameters was carried out considering the Mn_3Ga-like compound ($P6_3/mmc$ space group), with a stoichiometry similar to $(Fe_{2/3}Mn_{1/3})_3Si$, where Fe and Mn ions occupy the Mn site, while Si ions go into the Ga site. To deal with disorder, the Virtual Crystal Approximation was used[32]. The energy of the system for several values of the hexagonal lattice parameters (a and c) were determined by DFT calculations. The most relevant result is that there is a minimum of energy for a certain finite lattice parameter, say: $a = 5.05$ Å and $c = 4.12$ Å. See Fig. 5 (a) for the stoichiometric composition and (b) off-stoichiometric one. The cell parameters for those two cases are very similar and have a minor discrepancy in comparison to the experimental result: 4.7% for the a parameter and 10.0% for the c parameter. Considering the theoretical calculations were performed at zero Kelvin, while the experiments were performed at 300 K, with several approximations of the theoretical model, such as ignoring phonons, thermal expansion, compressibility and many other parameters, we consider the experimental-theoretical matching a strong indicator of the metastable nature of the experimentally observed hexagonal structure.

Our calculations, which assume a periodic unit cell, do not establish the mechanism for the stabilization of the metastable hexagonal phase in the prepared samples. Nevertheless, the preparation method kinetics, together with the final NP size induced strain/stress effects should be the main factors that lead to the stabilization of the metastable phase.

These DFT findings, presenting a minimum of energy for the hexagonal structure for the stoichiometric and off-stoichiometric full Heusler alloy, corroborates with our experimental results and support our ideas of a Heusler alloy with a new crystal phase, other than cubic and tetragonal.

4. Conclusion

In this paper we have produced NPs using PLD technique; and a core-shell pattern was found. The FFT, obtained from the TEM images clearly show an amorphous shell and a core with hexagonal crystal structure, determined after pattern matching. EDS measurements verify that the bulk target has a real composition close to

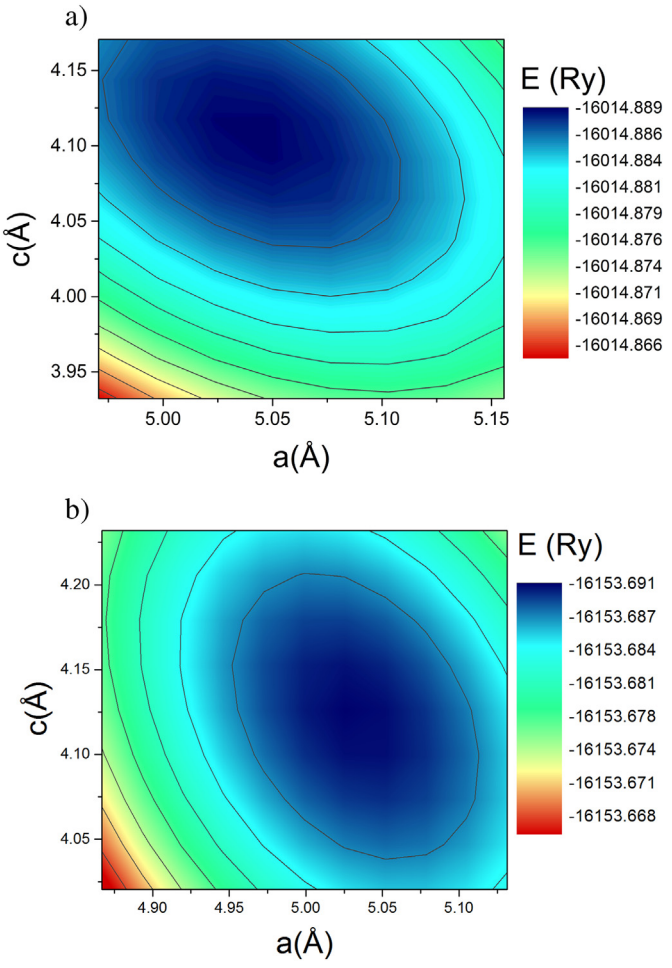

Fig. 5. Energy map as a function of hexagonal lattice parameters (a and c), for (a) stoichiometric and (b) off-stoichiometric Fe-Mn-Si full Heusler alloys, obtained from Density Functional Calculation (DFT).

the nominal one; while the core of the NPs are off-stoichiometric, with an iron-rich composition. DFT calculations corroborate with our findings, and shows that, in fact, a minimum of energy as a function of the hexagonal lattice parameters exists for stoichiometric and off-stoichiometric Fe-Mn-Si full Heusler alloys. We also performed magnetization measurements and the NPs, with hexagonal structure, present a quite different behavior in comparison to the bulk (target) counterpart; but these differences should be further explored elsewhere.

The properties of cubic and tetragonal Heusler alloys are well known to strongly depend on their magneto-structural interplay, leading to interesting physical properties such as magnetocaloric and magnetic memory shape effects. The discovery of a novel hexagonal structure for a full Heusler compound opens the way to the discovery and optimization of new materials properties and their potential applications.

Acknowledgments

MSR acknowledges FAPERJ, CAPES and CNPq (Brazil) for funding the research projects. MSR belongs to the INCT of *Refrigeração e Termofísica*, funding by CNPq by grant number 465448/2014-3. This work was developed within the scope of the project CICECO-Aveiro Institute of Materials, POCI-01-0145-FEDER-007679 (FCT Ref. UID/CTM/50011/2013), financed by national funds through the FCT/MEC and when appropriate co-financed by FEDER under the PT2020 Partnership Agreement. This work was also funded by FEDER funds through the COMPETE 2020 Programme and National Funds through FCT - Portuguese Foundation for Science and Technology under the project UID/CTM/50025/2013. JNG and JSA acknowledge FCT grants SFRH/BPD/82059/2011 and IF/01089/2015, respectively.

References

[1] V.V. Khovaylo, V.D. Buchelnikov, R. Kainuma, V.V. Koledov, M. Ohtsuka, V.G. Shavrov, T. Takagi, S.V. Taskaev, A.N. Vasiliev, Phase transitions in $Ni_{2+x}Mn_{1-x}Ga$ with a high Ni excess, Phys. Rev. B 72 (22) (2005) 224408.
[2] A.M. Tishin, Y.I. Spichkin, The Magnetocaloric Effect and Its Applications, CRC Press. 2016.
[3] Z.H. Liu, M. Zhang, Y.T. Cui, Y.Q. Zhou, W.H. Wang, G.H. Wu, X.X. Zhang, G. Xiao, Martensitic transformation and shape memory effect in ferromagnetic Heusler alloy Ni_2FeGa, Appl. Phys. Lett. 82 (3) (2003) 424–426.
[4] K. Ullakko, Magnetically controlled shape memory alloys: a new class of actuator materials, J. Mater. Eng. Perform. 5 (3) (1996) 405.
[5] A. Planes, L. Mañosa, M. Acet, Magnetocaloric effect and its relation to shape-memory properties in ferromagnetic heusler alloys, J. Phys. Condens. Matter 21 (23) (2009) 233201.
[6] C. Felser, G.H. Fecher, B. Balke, Spintronics: a challenge for materials science and solid-state chemistry, Angew. Chem. Int. Ed. 46 (5) (2007) 668–699.
[7] J. Winterlik, G.H. Fecher, A. Thomas, C. Felser, Superconductivity in ternary Heusler intermetallic compounds, Phys. Rev. B 79 (2009) 064–508.
[8] D. Kieven, R. Klenk, S. Naghavi, C. Felser, T. Gruhn, I-II-v half-heusler compounds for optoelectronics: ab initio calculations, Phys. Rev. B 81 (7) (2010) 075208.
[9] H. Lin, L.A. Wray, Y. Xia, S. Xu, S. Jia, R.J. Cava, A. Bansil, M.Z. Hasan, Half-Heusler ternary compounds as new multifunctional experimental platforms for topological quantum phenomena, Nat. Mater. 9 (7) (2010) 546–549.
[10] T. Graf, C. Felser, S.S.P. Parkin, Simple rules for the understanding of Heusler compounds, Prog. Solid State Chem. 39 (1) (2011) 1–50.
[11] E.V. Vidal, H. Schneider, G. Jakob, Influence of disorder on anomalous hall effect for heusler compounds, Phys. Rev. B 83 (17) (2011) 174410.
[12] X. Zhou, W. Li, H.P. Kunkel, G. Williams, A criterion for enhancing the giant magnetocaloric effect:(Ni-Mn-Ga)—a promising new system for magnetic refrigeration, J. Phys. Condens. Matter 16 (6) (2004) L39.
[13] V.K. Sharma, M.K. Chattopadhyay, A. Khandelwal, S.B. Roy, Martensitic transition near room temperature and the temperature-and magnetic-field-induced multifunctional properties of $Ni_{49}CuMn_{34}In_{16}$ alloy, Phys. Rev. B 82 (17) (2010) 172411.
[14] S. Khmelevskyi, A.V. Ruban, P. Mohn, Magnetic ordering and exchange interactions in structural modifications of Mn_3Ga alloys: interplay of frustration, atomic order, and off-stoichiometry, Phys. Rev. B 93 (18) (2016) 184404.
[15] W.Y. Zhang, P. Kharel, S. Valloppilly, R. Skomski, D.J. Sellmyer, Synthesis and magnetism of single-phase Mn-Ga films, J. Appl. Phys. 117 (17) (2015) 17E306.
[16] N. Yamada, H. Sakai, H. Mori, T. Ohoyama, Magnetic properties of -Mn_3Ge, Phys. B+C 149 (1988) 311–315.
[17] S. Tomiyoshi, Y. Yamaguchi, T. Nagamiya, Triangular spin configuration and weak ferromagnetism of Mn_3Ge, J. Magn. Magn. Mater. 31 (1983)630–629.
[18] K.V. Shanavas, M.A. McGuire, D.S. Parker, Electronic and magnetic properties of Si substituted Fe_3Ge, J. Appl. Phys. 118 (12) (2015) 123902.
[19] C. Wang, J. Meyer, N. Teichert, A. Auge, E. Rausch, B. Balke, A. Hütten, G.H. Fecher, C. Felser, Heusler nanoparticles for spintronics and ferromagnetic shape memory alloys, J. Vac. Sci. Technol., B: Nanotechnol. Microelectron.: Mater., Process., Meas., Phenom. 32 (2) (2014) 020802.
[20] R.J. Caraballo-Vivas, Magnetism From Intermetallics and Perovskite Oxides, 2017.arXiv preprint arXiv:1707.09868.
[21] L. Passoni, F. Giordano, S.M. Zakeeruddin, M. Grätzel, F.D. Fonzo, Hyperbranched self-assembled photoanode for high efficiency dye-sensitized solar cells, RSC Adv. 5 (113) (2015) 93180–93186.
[22] T.R. Garvey, B.H. Farnum, R. Lopez, Pulsed laser deposited porous nano-carpets of indium tin oxide and their use as charge collectors in core-shell structures for dye sensitized solar cells, Nanoscale 7 (6) (2015) 2400–2408.
[23] J.H. Noh, J.H. Park, H.S. Han, D.H. Kim, B.S. Han, S. Lee, J.Y. Kim, H.S. Jung, K.S. Hong, Aligned photoelectrodes with large surface area prepared by pulsed laser deposition, J. Phys. Chem. C 116 (14) (2012) 8102–8110.
[24] F.D. Fonzo, C.S. Casari, V. Russo, M.F. Brunella, A.L.i. Bassi, C.E. Bottani, Hierarchically organized nanostructured TiO_2 for photocatalysis applications, Nanotechnology 20 (1) (2008) 015604.
[25] Y. Li, T. Sasaki, Y. Shimizu, N. Koshizaki, Hexagonal-close-packed, hierarchical amorphous TiO_2 nanocolumn arrays: transferability, enhanced photocatalytic activity, and superamphiphilicity without UV irradiation, J. Am. Chem. Soc. 130 (44) (2008) 14755–14762.
[26] Y. Hara, T. Garvey, L. Alibabaei, R. Ghosh, L. Rene, Controlled seeding of laser deposited Ta: TiO_2 nanobrushes and their performance as photoanode for dye sensitized solar cells, ACS Appl. Mater. Interfaces 5 (24) (2013) 13140–13145.
[27] Y. Wang, A. Tabet-Aoul, M. Mohamed, Laser synthesis of hierarchically organized nanostructured TiO_2 films on microfibrous carbon paper substrate: characterization and electrocatalyst supporting properties, J. Power Sources 299 (2015) 149–155.
[28] L. Passoni, L. Criante, F. Fumagalli, F. Scotognella, G. Lanzani, F.D. Fonzo, Self-assembled hierarchical nanostructures for high-efficiency porous photonic crystals, ACS Nano 8 (12) (2014) 12167–12174.
[29] N.R. Checca, R.J. Caraballo-Vivas, R. Torrao, A. Rossi, M.S. Reis, Phase composition and growth mechanisms of half-metal Heusler alloy produced by pulsed laser deposition: from core-shell nanoparticles to amorphous randomic clusters, Mater. Chem. Phys. 196 (2017) 103–108.
[30] J.P. Perdew, K. Burke, M. Ernzerhof, Generalized gradient approximation made simple, Phys. Rev. Lett. 77 (1996) 3865–3868.
[31] P. Blaha, K. Schwarz, G.K.H. Madsen, D. Kvasnicka, J. Luitz, WIEN2K, An Augmented Plane Wave+ Local Orbitals Program for Calculating Crystal Properties, 2001.
[32] L. Nordheim, Zur elektronentheorie der metalle. i, Ann. Phys. 401 (5) (1931) 607–640.
[33] D.R.G. Mitchell, B. Schaffer, Scripting-customised microscopy tools for digital micrograph, Ultramicroscopy 103 (4) (2005) 319–332.
[34] P.A. Stadelmann, EMS - a software package for electron diffraction analysis and HREM image simulation in materials science, Ultramicroscopy 21 (2) (1987) 131–145.
[35] S.S. Pedro, R.J. Caraballo Vivas, V.M. Andrade, C. Cruz, L.S. Paixao, C. Contreras, T. Costa-Soares, L. Caldeira, A.A. Coelho, A. Carvalho, G. Magnus, D.L. Rocco, M.S. Reis, Effects of Ga substitution on the structural and magnetic properties of half metallic Fe_2MnSi Heusler compound, J. Appl. Phys. 117 (1). (2015)
[36] J.C.G. Tedesco, S.S. Pedro, R.J. Caraballo Vivas, C. Cruz, V.M. Andrade, A.M. Dos Santos, A.M.G. Carvalho, M. Costa, P. Venezuela, D.L. Rocco, Chemical disorder determines the deviation of the Slater-Pauling rule for Fe_2MnSi-based Heusler alloys: evidences from neutron diffraction and density functional theory, J. Phys. Condens. Matter 28 (47) (2016) 476002.
[37] H. Mamiya, M. Ohnuma, I. Nakatani, T. Furubayashim, Extraction of blocking temperature distribution from zero-field-cooled and field-cooled magnetization curves, IEEE Trans. Magn. 41 (10) (2005) 3394–3396.